




## In situ TEM characterisation of dislocation interactions in $\alpha$ -titanium

Josh Kacher & Ian M. Robertson


To cite this article: Josh Kacher & Ian M. Robertson (2016) In situ TEM characterisation of dislocation interactions in  $\alpha$ -titanium, Philosophical Magazine, 96:14, 1437-1447, DOI: [10.1080/14786435.2016.1170222](https://doi.org/10.1080/14786435.2016.1170222)

To link to this article: <https://doi.org/10.1080/14786435.2016.1170222>

 View supplementary material 

 Published online: 04 Apr 2016.

 Submit your article to this journal 

 Article views: 537

 View related articles 

 View Crossmark data 

 Citing articles: 4 View citing articles 



## *In situ* TEM characterisation of dislocation interactions in $\alpha$ -titanium

Josh Kacher<sup>a</sup> and Ian M. Robertson<sup>b</sup>

<sup>a</sup>Department of Materials Science and Engineering, Georgia Institute of Technology, Atlanta, GA, USA;

<sup>b</sup>Department of Materials Science and Engineering, College of Engineering, Madison, WI, USA

### ABSTRACT

*In situ* straining in the transmission electron microscope and diffraction-contrast electron tomography has been applied to investigate dislocation interactions in  $\alpha$ -Ti. Dislocation debris, in the form of small loops, was seen to form from sequential cross-slip events. Electron tomography provided direct three-dimensional visualisation of the dislocation structures, allowing accurate identification of slip planes, dislocation line directions and spatial relations between dislocations.

### ARTICLE HISTORY

Received 24 August 2015

Accepted 20 March 2016

### KEYWORDS

Titanium; transmission electron microscopy; *in situ* electron microscopy; dislocation interactions

## 1. Introduction

The most common slip mode in  $\alpha$ -Ti at room temperature is prismatic slip of  $\langle a \rangle$ -type dislocations, or  $\langle 11\bar{2}0 \rangle \{1\bar{1}00\}$ . Basal and pyramidal slip are much less common, though Naka et al. have reported a temperature regime between 300 and 500 K where cross-slip between the prismatic and first-order pyramidal planes becomes active [1,2]. They reported that this cross-slip behaviour contributes to an anomaly in the critically resolved shear stress over a similar temperature regime. Transmission electron microscopy (TEM), including *in situ* TEM deformation, studies have shown that dislocation interactions in this regime undergo double cross-slip events, in which screw dislocations periodically slip between the prismatic and pyramidal slip planes [3–6]. High-resolution electron microscopy and atomistic computer simulations have suggested this cross-slip behaviour is caused by limited spreading of the core of screw dislocations between the prismatic and pyramidal planes, resulting in cross-slip events in the absence of any observable obstacle to dislocation motion [7–9]. This is suspected, though not confirmed, to be due to the influence of oxygen on the dislocation core structure. *Post mortem* TEM characterisation of deformed  $\alpha$ -Ti and Zr has shown the presence of dislocation debris in the form of dipoles or small loops [1,3]. While this has been attributed to dislocation cross-slip, this mechanism of debris formation has not been observed directly.

**CONTACT** Josh Kacher ✉ [josh.kacher@mse.gatech.edu](mailto:josh.kacher@mse.gatech.edu)

Supplemental data for this article can be accessed at <http://dx.doi.org/10.1080/14786435.2016.1170222>.

© 2016 Informa UK Limited, trading as Taylor & Francis Group

In this paper, results obtained using *in situ* TEM deformation and *post mortem* characterisation of the deformed state are presented to elucidate dislocation/dislocation interactions in commercially pure  $\alpha$ -Ti. To aid in the analysis and interpretation of the interactions, a recently developed electron microscopy technique in which *in situ* TEM deformation experiments are combined with three-dimensional snapshots was employed [10]. This combination allows the evolution of the microstructure to be followed in real time and the analysis to be conducted three-dimensionally and represents a shift towards four-dimensional characterisation of defect structures [11].

## 2. Experimental methods

Commercially pure  $\alpha$ -Ti was used in this study. The deformation processes were investigated in a JEOL 2010 LaB<sub>6</sub> TEM operated at an accelerating voltage of 200 kV. A Gatan model deformation/heating stage that allows samples to be deformed under tension *in situ* at displacement rates up to 1  $\mu\text{m/s}$  and at temperatures up to 1000°C was used. Geometrical constraints limit tilting of the Gatan stage to  $\pm 35^\circ$  about a single axis. Samples were prepared for characterisation in the TEM by first shearing them to stage-specified dimensions, 11.5  $\times$  2.5-mm bars for use in the deformation stage. These were mechanically ground to an approximate thickness of 200  $\mu\text{m}$ . Final thinning to electron transparency was achieved using a twin jet polisher with a 6% perchloric acid, 39% butanol and 55% methanol electrolyte maintained at a temperature of  $-30^\circ\text{C}$ .

*In situ* TEM deformation was conducted at room temperature. The samples were deformed at a displacement rate of 1  $\mu\text{m/s}$  until dislocation motion was observed. Once dislocation motion was initiated, stage displacement was stopped and the system allowed to relax. Further deformation was induced periodically to reinitiate the dislocation motion. Dislocation motion and behaviour was recorded using a charged couple device camera at a frame rate of 10 frames per second.

Diffraction-contrast electron tomography was used to generate 3D representations of the dislocation state. The procedure for reconstructing tomograms of defect interactions has been described in detail elsewhere [12,13], but it is important to note that generally, diffraction contrast electron tomography requires a stage with at least two axes of tilt to maintain consistent diffraction contrast conditions during image acquisition over a wide angular range. The alignment and reconstruction stages of electron tomography were carried out using the EM3D software package (<http://em3d.stanford.edu/>) and UCSF Chimera [14] was used for visualisation of the tomogram. Once reconstructed, the tomogram served as the basis for the construction of a 3D-dislocation model. A real space coordinate system in the form of a hexagonal lattice was also included in the 3D model and was aligned with the crystal lattice orientation using diffraction data collected in the TEM. Using the tomogram as a basis for constructing a 3D model combined with prior knowledge about the properties of dislocations and image contrast theory has allowed a significant reduction in the number of images and angular range required for the full 3D characterisation of a system in comparison to traditional electron tomography [13]. This reduction in the number of required images was essential to enable 4D characterisation of dislocation–obstacle interactions.

Diffraction-contrast electron tomography was coupled with the dynamic dislocation information by interrupting the *in situ* TEM straining and collecting a series of images at regular tilt intervals, generally  $1^\circ$ , over the allowable angular range of the stage. As the

tilting was not about a specific direction or along a particular Kikuchi band, the diffraction conditions were not kept constant and consequently the image contrast fluctuated strongly between images; maintaining the same diffraction condition and minimising the image-to-image fluctuation are normally taken as requirements in electron tomography. To overcome the attendant difficulties in image alignment and tomographic reconstruction that results from fluctuating image-to-image contrast, knowledge that dislocations cannot end in the interior but at an intersection with an interface was used to mark manually the point of intersection of the dislocation with the free surface. These digital markers were used to facilitate image alignment and appeared as spheres marking the location of dislocation intersection with the foil surface in the reconstructed tomogram. Faint dislocation contrast and the location of the spheres in the tomogram provided sufficient information to construct a high-fidelity 3D-dislocation model of the interaction. This approach to electron tomography of dislocation structures is described in more detail elsewhere [10,15].

### 3. Results

An example of a dislocation interacting with an obstacle is shown in the time series of images presented in Figure 1; the video of the interaction is provided in supplemental information (Suppl. Vid. 1). To aid the description of the time-resolved series of images presented in Figure 1, key components of the interaction are shown schematically in Figure 1(i); here the letters correspond to the appropriate frame of Figure 1(a)–(e). The two planes are coloured black and red, with corresponding shading used to denote the plane on which the dislocation segment resides. The dislocation of interest is indicated by an arrowhead and its direction of motion is indicated by an arrow (Figure 1(a). In Figure 1(b), an interior section of the dislocation cross-slipped though no obstacle is seen in the micrograph, resulting in the formation of a sessile segment. As stress continued to act on the dislocation, the dislocation components on either side of the pinned segment moved independently and bowed under the applied stress (Figure 1(c)). As these dislocation segments expanded, one encountered the foil surface and caused the dislocation to separate into a single glissile dislocation and a half-loop connected to the foil surface (Figure 1(d)). The half-loop continued to expand (Figure 1(e)–(f)) and, as the interaction occurred in a thin foil, it separated into two independent dislocations on intersecting the foil surface (Figure 1(g)). These three dislocation segments are labelled ‘1’, ‘2’ and ‘3’ in Figure 1(h). The final state of the interaction left one dislocation propagating in the original direction on the original slip plane (dislocation 1), one dislocation propagating in the same direction but on a parallel slip plane (dislocation 2) and one dislocation propagating in the opposite direction but with components on both slip planes presumably connected by a jogged segment (dislocation 3). Using the surface slip traces of the glissile dislocations, the distance in projection between the two slip planes was measured as 73.5 nm (Figure 1(g) *inset*). Assuming the glide and cross-slip planes were the prismatic and pyramidal, respectively, this projected distance corresponds to an actual distance of 33.8 nm between the slip planes of the glissile dislocations. Analysis shown in the following example will justify this choice in assumed primary and secondary slip planes.

Cross-slip events and the resultant half-loop generation similar to that shown in Figure 1 were commonly observed during the *in situ* TEM deformation experiments, but the behaviour of the generated half-loops varied depending on the distance between the parallel glide planes of the dislocation segments. This is demonstrated in Figure 2 in which glissile

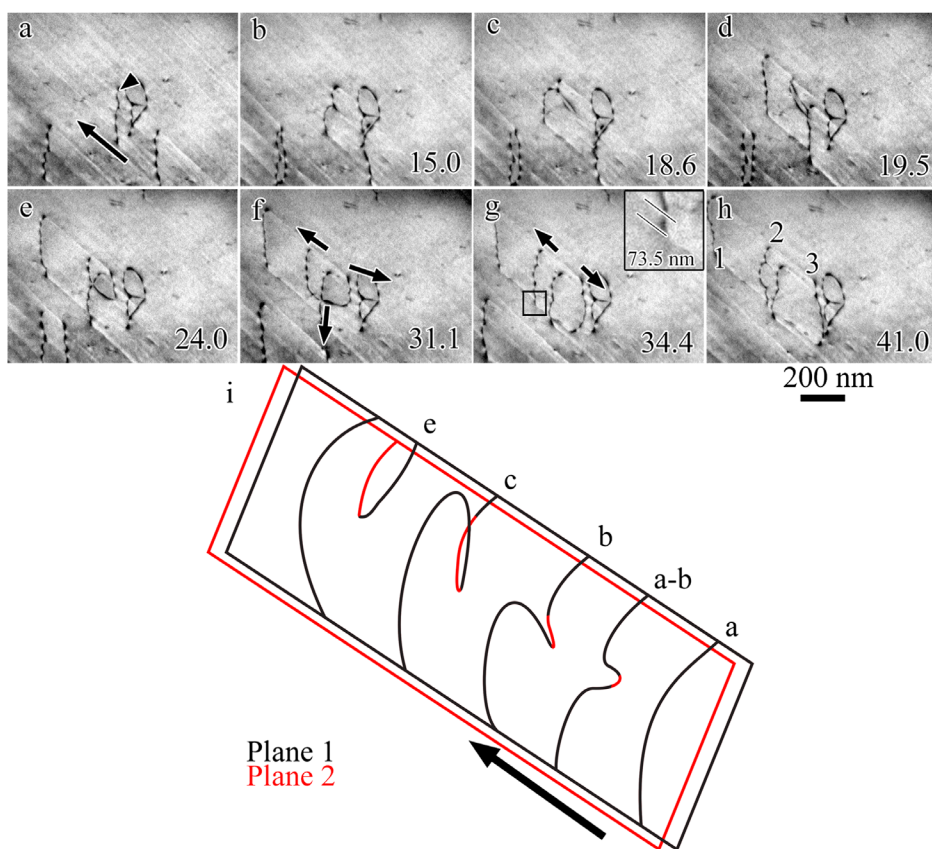


**Figure 1.** (colour online) Frames taken from a video during *in situ* straining of  $\alpha$ -Ti at room temperature showing dislocation generation through cross-slip mechanisms (a)–(h) with accompanying schematic (i). Dislocation segments are shaded in accordance with their habitat planes, with the black plane nearer the reader. The letter labels correlate the schematic with the video frame. Arrows show the direction of motion. The dislocation of interest is indicated in the first panel. Numbering (h) is for reference in the text. The inset in (g) highlights the slip traces of two of the dislocation segments, showing that they reside on different slip planes. The experiment time is given in each panel in seconds.

dislocations are seen interacting with an array of sessile dislocations during *in situ* TEM straining; the video of the interaction is provided as Suppl. Vid. 2. The lead dislocation, labelled 1 in Figure 2(b), bowed slightly as it intersected an immobile dislocation. As the glissile dislocation passed through the field of view, small loops and half loops separated from the dislocation and remained in the matrix as dislocation debris. The remnant dislocation debris from the passage of the dislocation is indicated in Figure 2(f) with arrowheads. As can be seen, the passage of a single dislocation through the field of view generated three distinct pieces of dislocation debris. This debris is far removed from the interaction with the sessile dislocation, suggesting that it arises from interactions of the dislocation with other obstacles distributed throughout the matrix or as a result of an intrinsic dislocation state, similar to the interaction shown in Figure 1. Unlike the half-loop generated in the interaction shown in Figure 1, the half-loops in the interaction shown in Figure 2 did not expand and remained significantly smaller. Additionally, full loops in the foil interior were



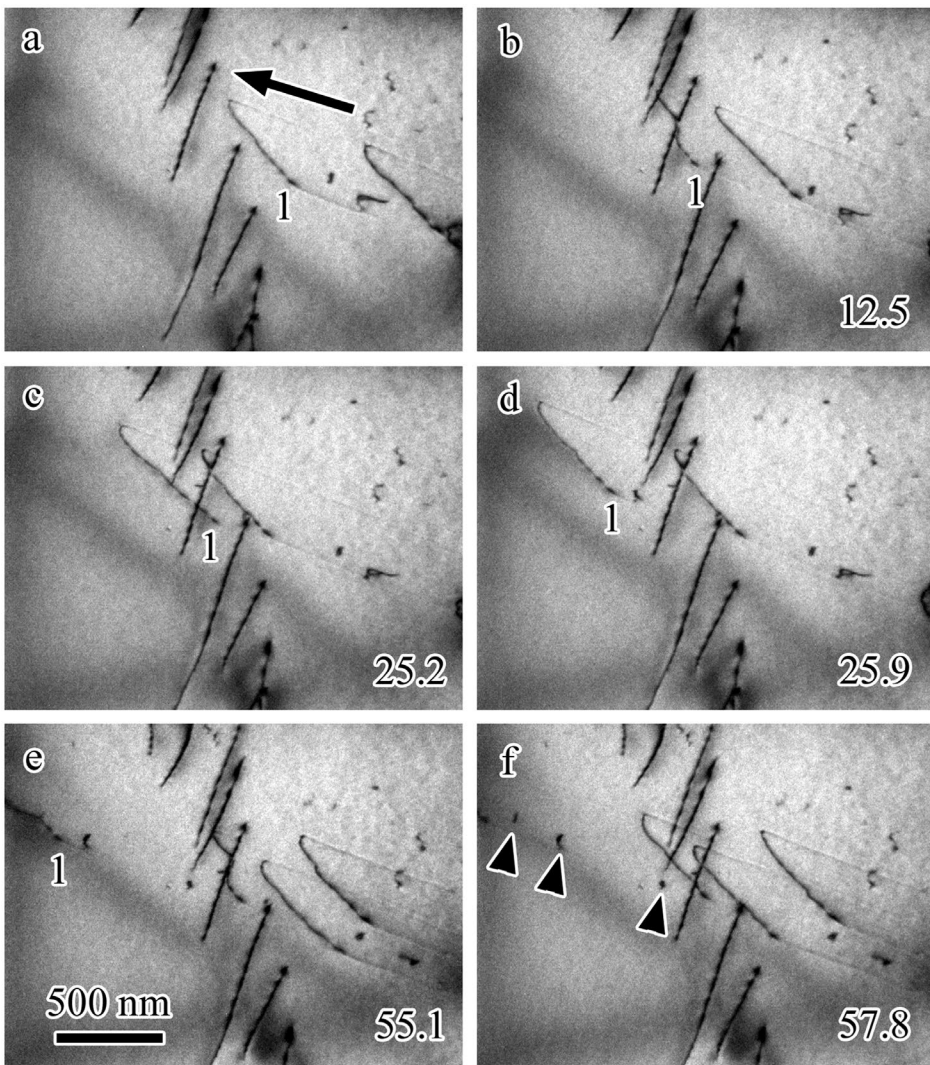


**Figure 2.** Glissile dislocations interacting with a dislocation array in  $\alpha$ -Ti during *in situ* straining at room temperature. The arrow in (a) indicates the direction of dislocation motion. Dislocation debris created by the gliding dislocation is indicated by arrowheads in (f). The lead dislocation is indicated by '1' for reference in the text. Experiment time is given in each panel in seconds.

also generated which would require the non-cross-slip dislocation segments to reconnect and pinch off the cross-slip section. This is likely due to the initial cross-slip distance being smaller such that the two dislocation segments, which are of opposite type, can recombine.

In order to relate the size of the generated loops to the subsequent expansion behaviour, the cross-slip step height was measured for 12 different cross-slip events that resulted in the generation of a loop or half-loop, including the three indicated in Figure 2 as well as the one shown in Figure 1. To accurately account for projection effects in the measurements, the cross-slip plane must be known. For this reason, and to gain a greater understanding of the spatial relationship of the dislocations and the attendant debris, electron tomography

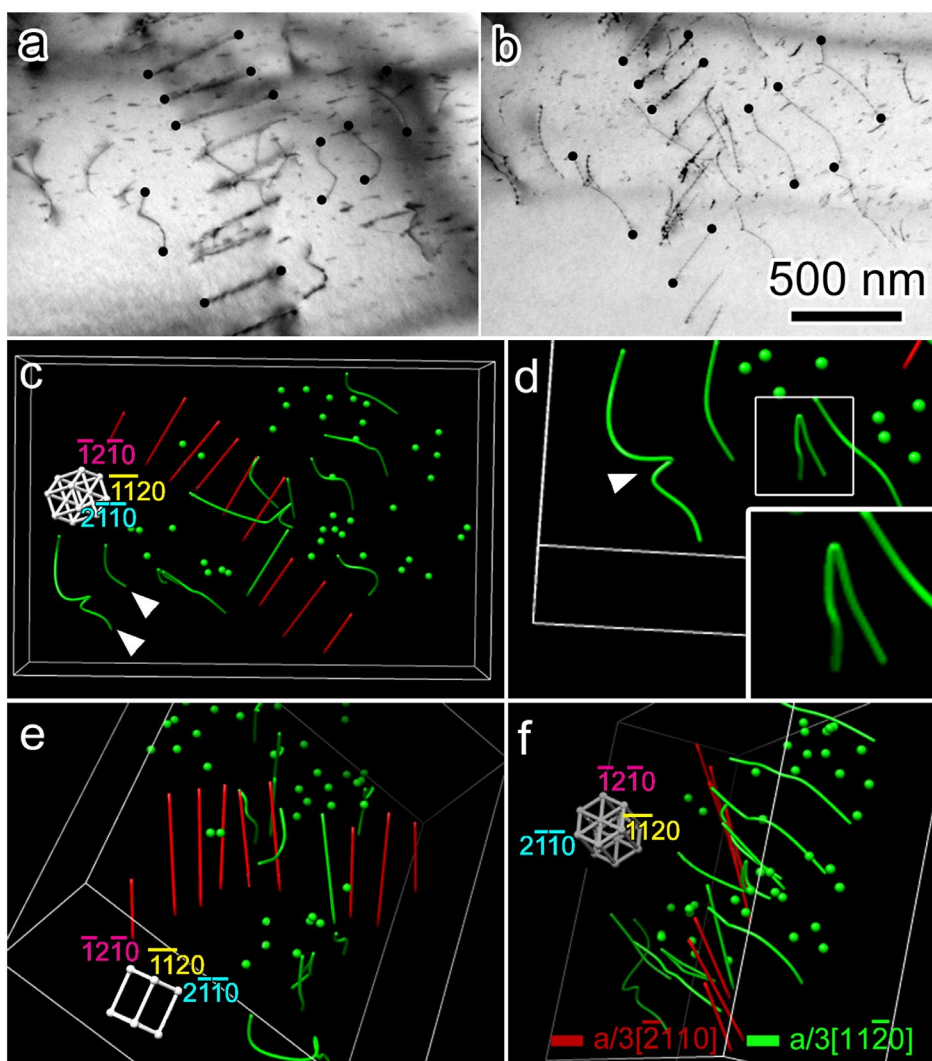


**Figure 3.** (colour online) (a)–(b) Images from tilt series from the interaction shown in Figure 2. Digital fiducial markers manually added to aid in alignment are also included. Stage tilt is given in each image. (c)–(f) Views of the 3D-dislocation model constructed of the interaction. Dislocations glissile on the pyramidal plane are indicated by arrowheads in (c). A kinked dislocation is indicated by an arrowhead and an enlarged view of a dislocation half-loop attached to the foil surface is given in (d). ‘a’ directions are colour coded for convenience. (For interpretation of the references to colour in this figure, the reader is referred to the web version of this article.).

was used. As the dislocation dynamics were revealed during an *in situ* straining experiment, the fiducial marker method was used to construct the tomogram and subsequent model [10]. Figure 3 shows two example electron micrographs from the collected tilt series along with the fiducial markers for the interaction shown in Figure 2. Different views of the constructed 3D-dislocation model are shown in Figure 3(c)–(f) along with the real-space coordinate system. The gliding dislocations shown were identified using conventional  $\mathbf{g} \cdot \mathbf{b}$

analysis to have a Burgers vector  $\mathbf{b} = \pm a/3 [1\ 1\ \bar{2}\ 0]$  and the immobile dislocations to have a Burgers vector  $\mathbf{b} = \pm a/3 [\bar{2}\ 1\ 1\ 0]$ .

The dislocation model shows the main gliding dislocations, coloured grey in the model (green in online version), to slip on and near  $(1\ \bar{1}\ 0\ 0)$  and have a line direction near parallel to  $[1\ 1\ \bar{2}\ 0]$ , making them pure screw dislocations gliding on the prismatic plane; this can be determined by the information contained in Figure 3(e) and the direction of glide observed in Supplementary Video 2. The cross-slipped segments reside on  $(\bar{1}\ 1\ 0\ 1)$ , or the pyramidal plane. A limited number of dislocations exhibited the reverse behaviour; the dislocations were glissile on a pyramidal plane and cross-slipped onto a prismatic plane (examples are indicated by arrowheads in Figure 3(c)). The immobile dislocations, coloured white (red in online version) in the model, resided on  $(1\ \bar{2}\ 1\ 0)$  and had an approximate line direction of  $[\bar{1}\ 2\ \bar{1}\ 1]$ , making them mixed-character sessile dislocations. This interpretation is consistent with the observed behaviour during the *in situ* TEM straining experiments (Figure 3). Other features of note in the tomogram include numerous small dislocation loops interspersed evenly throughout the foil (represented as grey spheres in the model, green in the online version), half-loops connected to the foil surface (Figure 3(d)) and kinks forming on the gliding dislocations (Figure 3(d)).

Full characterisation of the dislocations enables identification of the changes to the gliding dislocations from intersecting the sessile dislocations. The intersection of the two dislocation types shown in Figures 2–3 should result in a jog forming on the gliding dislocations with a line direction parallel to the  $[\bar{2}\ 1\ 1\ 0]$  direction. These jogs should still be glissile on the basal plane, but require climb and the emission of vacancies for glide on the prismatic or pyramidal planes, thus impeding further propagation of the dislocations. This impediment to motion is visible in Figures 2(b) and (e) as the glissile dislocations are temporarily arrested at the sessile dislocations. However, as the dislocations propagated through the matrix, it appears that cross-slip played a larger role in the dislocation behaviour than interactions with sessile dislocations.

Though the barrier to dislocation motion presented by the cross-slip activity varies with the length of the cross-slip segment (jog), comparison of the relative barrier strengths associated with dislocation intersections and cross-slip is instructive. To do so, the radius of curvature of dislocation 1 from Figure 2 was measured as it interacted with a sessile dislocation (Figure 2(b)) and directly before coming into contact with the foil surface after a cross-slip event (two instances: between Figure 2(c) and (d) and between Figure 2(d) and (e)) using a method similar to that used by Caillard et al. [16]. It was found that the radius of curvature is approximately three times greater when the dislocation interacts with a sessile dislocation than after undergoing cross-slip (765 nm vs. 264 nm). The radius of curvature of the dislocation is related to the stress acting on the dislocation (or the barrier strength of an obstacle if this measurement is made directly before overcoming the obstacle) by the formula:  $\tau = \mu b/R$ , where  $\tau$  is the resolved shear stress acting on the dislocation,  $\mu$  is the shear modulus and  $R$  is the radius of curvature of the dislocation. In this case then, the barrier to dislocation propagation from the cross-slip activity was three times higher than that presented by the sessile dislocations.

With the dislocation slip planes known, projection effects can be accounted for and the distance between the slip planes associated with the cross-slip events can be measured and calculated. All of the analysed cross-slip events resulted in a half-loop attached to the foil surface. Of those, eight of the half-loops expanded towards the opposite foil surface and



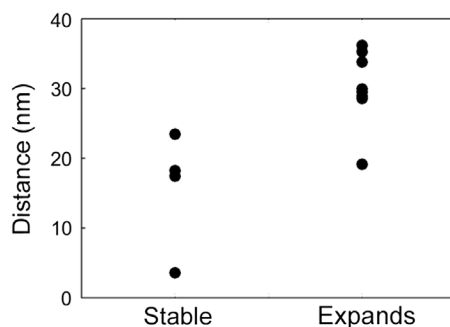


**Figure 4.** Distance between cross-slip planes compared to observed dislocation half-loop behaviour. 'Expands' refers to half-loops that expand and come in contact with the opposite foil surface and 'Stable' refers to half-loops that remain small.

four remained stable. For the stable four half-loops, the separation distance between the dislocation segments, the cross-slip distance, ranged from 3.6 to 23.5 nm with an average of 15.7 nm. The cross-slip distance associated with the expanding half-loops ranged from 19.1 to 36.2 nm with an average 30.2 nm (data displayed graphically in Figure 4).

#### 4. Discussion

A central feature of dislocation motion observed during deformation of  $\alpha$ -Ti was the prevalence of cross-slip events, the majority of which occurred between the prismatic and pyramidal planes. Similar cross-slip activity has been inferred after *post mortem* characterisation of deformed Ti [3] and seen during *in situ* TEM deformation of  $\alpha$ -Ti [5], Ti-6Al-4V [6] and Zr at elevated temperatures [16]. Naka et al. reported that even when single crystal samples were oriented for prismatic glide, cross-slip between the prismatic and first order pyramidal planes occurred. The occurrence of cross-slip events was heterogeneously distributed along the length of  $\langle a \rangle$ -type screw dislocations, likely reflecting a distribution in both size and position of barriers to dislocation motion. These barriers could not be resolved during TEM characterisation. To explain this behaviour, Naka et al. proposed a model in which the core of  $\langle a \rangle$ -type screw dislocations was spread between both the prismatic and the pyramidal planes, promoting cross-slip of dislocation segments onto the pyramidal planes. As the prismatic plane is the most energetically favourable for glide in  $\alpha$ -Ti, further applied stress would cause the dislocation segment on the pyramidal plane to cross-slip back onto the prismatic plane. This cross-slip could either return the dislocation to its original glide plane or result in the dislocation being split between two parallel prismatic planes with a connecting sessile segment.

Farenc et al. conducted a series of low-temperature *in situ* TEM deformation tests on  $\alpha$ -Ti to further explore the phenomena described by Naka et al. [5]. They found that screw dislocations moved via a locking/unlocking mechanism and hypothesised that the screw dislocation cores switched between a less stable glissile configuration, defined by core spreading on the prismatic plane, and a more stable sessile configuration with core spreading occurring on the pyramidal plane. In agreement with Naka et al., they presumed that the presence of solutes such as oxygen could affect the core structure of the dislocations,

further stabilising the sessile configuration. Clouet et al. supported this hypothesis with first principle calculations, showing that the electronic structure of screw dislocations in  $\alpha$ -Ti favours the sessile configuration over the glissile one [9]. Castany et al. observed similar behaviour of dislocations in the  $\alpha$  phase of Ti-6Al-4V, attributing the dragging behaviour of the dislocations to core spreading onto glissile planes [6].

Couret [17], Caillard et al. [16], Moon et al. [18] observed similar dislocation cross-slip and jog formation activity but in  $\gamma$ -TiAl, a Zr alloy and Zircaloy-4, respectively. Couret attributed the dislocation pinning to extrinsic barriers distributed throughout the matrix, possibly oxygen clusters, as opposed to the intrinsic obstacles proposed by groups investigating dislocation behaviour in  $\alpha$ -Ti [6,9]. Caillard suggested solute drag as a determining factor in the behaviour of dislocation cross-slip segments. TEM analysis by Moon et al. revealed similar dislocation debris generated behind dislocations as was reported in this study. They categorised different dislocation configurations according to the height of super-jog segments connecting dislocation segments after cross-slip and found that this height was an important factor when modelling creep behaviour of their material.

Investigations of the core structure of  $\langle a \rangle$ -type screw dislocations in  $\alpha$ -Ti have suggested limited spreading of the dislocation core, though the exact structure is still being debated [1,7,8,19]. Neeraj et al. found that  $\alpha$ -Ti displays asymmetric behaviour between deformation in tension and compression [8]. This asymmetry was attributed to the behaviour of  $\langle a \rangle$ -type dislocations, which were found to readily cross-slip during tensile deformation. High-resolution electron microscopy of  $\langle a \rangle$ -type edge dislocations has shown slight spreading of the dislocation core onto the pyramidal plane, suggesting a similar cross-slip mechanism as that proposed by Naka et al. [7]. Girshick et al. investigated the core structure of  $\langle a \rangle$ -type screw dislocations in Ti using atomistic simulations [19]. Similar to the conclusions of Naka et al., they observed non-planar core spreading, though this spreading occurred mainly between the prismatic and basal planes. As the core spreading affects which planes the dislocations are most likely to cross-slip onto, comparison with the results shown in this study is useful for verification. The *in situ* TEM straining results reported in this study and previously reported *in situ* investigations [5,6] are supportive of dislocation core spreading on the pyramidal and prismatic planes.

During the *in situ* deformation reported in this study, dislocation cross-slip was seen to generate both small loops fully enclosed in the thin films as well as larger half-loops connected to the foil surface. The reason for this cross-slip behaviour, either intrinsic barriers as suggested by Clouet et al. [9] and Castany et al. [6] or dispersed extrinsic barriers as suggested by Couret [17], could not be determined from the *in situ* TEM deformation experiments though the variations in the dislocation behaviour suggests that an external influence such as solute oxygen plays a role. Obstacle barrier strength (either intrinsic or extrinsic), proximity to foil surface, local stress state and the location of the slip plane with respect to the obstacle could account for the different dislocation reactions as they likely affect the length of the cross-slip segment (Figure 2). Larger barriers to dislocation motion could lead to the formation of the expanding half-loops and the multiplication of glissile dislocations, such as is seen in Figure 1, while smaller barriers result in a distribution of loops and half-loops, such as is seen in Figure 2. Electron tomography of the deformed regions showed that dislocation loops were distributed throughout the foil thickness, suggesting that their formation is not due to surface effects. Electron tomography was also instrumental in identifying the dominant slip planes of cross-slipped dislocation segments

that lead to the formation of dislocation loops. The *in situ* TEM deformation experiments also showed that the dislocations can repeatedly generate dislocation loops and half-loops during glide (Figure 2). This sequential generation of loops and half loops during dislocation glide has not been reported in other studies of  $\alpha$ -Ti, but could present a significant source of dislocation debris, impeding the glide of trailing dislocations and contributing to work hardening during deformation.

## 5. Conclusion

Dislocation generation through cross-slip mechanisms, previously suggested from *post mortem* observations, was observed in real time during *in situ* deformation of  $\alpha$ -Ti. Single gliding dislocations were seen undergoing multiple cross-slip events, resulting in the sequential emission of loops and half-loops. Tomographic analysis of the dislocation interactions showed the dislocations to cross-slip primarily between the prismatic and first order pyramidal planes.

## Disclosure statement

No potential conflict of interest was reported by the authors.

## Funding

This work was supported by the US Department of Energy Office of Basic Energy Sciences, Division of Materials Science [award number DEFG-02-07ER46443]; the microscopy was carried out in the Frederick Seitz Materials Research Laboratory Central Facilities, University of Illinois.

## Notes on contributors

**Josh Kacher** is an Assistant Professor having interests in mechanical behaviour of materials and materials in extreme environments.

**Ian Robertson** is Dean of College of Engineering having interests in mechanical behaviour of materials and materials in extreme environments

## References

- [1] S. Naka, A. Lasalmonie, P. Costa, and L.P. Kubin, The low-temperature plastic deformation of  $\alpha$ -titanium and the core structure of a-type screw dislocations, *Philos. Mag. A* 57 (1988), pp. 717–740.
- [2] A.T. Churchman, The slip modes of titanium and the effect of purity on their occurrence during tensile deformation of single crystals, *Proc. R. Soc. London, Ser. A* 226 (1954), pp. 216–226.
- [3] S. Naka and A. Lasalmonie, Cross-slip on the first order pyramidal plane (1011) of a-type dislocations (1210) in the plastic deformation of  $\alpha$ -titanium single crystals, *J. Mater. Sci.* 18 (1983), pp. 2613–2617.
- [4] U. Messerschmidt and M. Bartsch, Generation of dislocations during plastic deformation, *Mater. Chem. Phys.* 81 (2003), pp. 518–523.
- [5] S. Farenc, D. Caillard, and A. Couret, An *in situ* study of prismatic glide in  $\alpha$  titanium at low temperatures, *Acta Metall. Mater.* 41 (1993), pp. 2701–2709.

- [6] P. Castany, F. Pettinari-Sturmel, J. Crestou, J. Douin, and A. Coujou, Experimental study of dislocation mobility in a Ti-6Al-4V alloy, *Acta Mater.* 55 (2007), pp. 6284–6291.
- [7] A. de Crecy, A. Bourret, S. Naka, and A. Lasalmonie, High resolution determination of the core structure of 1/31120{1010} edge dislocation in titanium, *Philos. Mag. A* 47 (1983), pp. 245–254.
- [8] T. Neeraj, M.F. Savage, J. Tatalovich, L. Kovarik, R.W. Hayes, and M.J. Mills, *Observation of tension-compression asymmetry in  $\alpha$  and  $\alpha/\beta$  titanium alloys*, *Philos. Mag.* 85 (2005), pp. 279–295.
- [9] E. Clouet, D. Caillard, N. Chaari, F. Onimus, and D. Rodney, Dislocation locking versus easy glide in titanium and zirconium, *Nat. Mater.* 14 (2015), pp. 931–936.
- [10] J. Kacher and I.M. Robertson, Quasi-four-dimensional analysis of dislocation interactions with grain boundaries in 304 stainless steel, *Acta Mater.* 60 (2012), pp. 6657–6672.
- [11] J. Kacher, B. Cui, and I.M. Robertson, *In situ* and tomographic characterization of damage and dislocation processes in irradiated metallic alloys by transmission electron microscopy, *J. Mater. Res.* 30 (2015), pp. 1202–1213.
- [12] J.S. Barnard, J. Sharp, J.R. Tong, and P.A. Midgley, Electron tomography of dislocations, *Microsc. Microanal.* 13 (2007), pp. 150–151.
- [13] G.S. Liu and I.M. Robertson, Three-dimensional visualization of dislocation-precipitate interactions in a Al-4Mg-0.3Sc alloy using weak-beam dark-field electron tomography, *J. Mater. Res.* 26 (2010), pp. 514–522.
- [14] E.F. Pettersen, T.D. Goddard, C.C. Huang, G.S. Couch, D.M. Greenblatt, E.C. Meng, and T.E. Ferrin, UCSF Chimera - a visualization system for exploratory research and analysis, *J. Comput. Chem.* 25 (2004), pp. 1605–1612.
- [15] J. Kacher and I.M. Robertson, *In situ* and tomographic analysis of dislocation/grain boundary interactions in  $\alpha$ -titanium, *Philos. Mag.* 94 (2014), pp. 814–829.
- [16] D. Caillard, M. Rautenberg, and X. Feaugas, Dislocation mechanisms in a zirconium alloy in the high-temperature regime: An *in situ* TEM investigation, *Acta Mater.* 87 (2015), pp. 283–292.
- [17] A. Couret, An *in-situ* study of ordinary dislocation glide in  $\gamma$ -TiAl alloys, *Philos. Mag. A* 79 (1999), pp. 1977–1994.
- [18] J.H. Moon, P.E. Cantonwine, K.R. Anderson, S. Karthikeyan, and M.J. Mills, Characterization and modeling of creep mechanisms in Zircaloy-4, *J. Nucl. Mater.* 353 (2006), pp. 177–189.
- [19] A. Girshick, D.G. Pettifor, and V. Vitek, Atomistic simulation of titanium. II. Structure of 1/3 screw dislocations and slip systems in titanium, *Philos. Mag. A* 77 (1998), pp. 999–1012.